Title

Pressure-induced suppression of Jahn–Teller distortions and enhanced electronic properties in high-entropy oxide (Mg0.2Ni0.2Co0.2Zn0.2Cu0.2)O

Journal

Applied Physics Letters, 119(15)

ISSN

0003-6951

Authors

Yan, Jiejuan
Zhang, Lingkong
Liu, Junxiu
et al.

Publication Date

2021-10-11

DOI

10.1063/5.0067432

Peer reviewed

Pressure Engineering of Jahn-Teller Distortion and Electronic Structure in High-Entropy Oxide $(Mg_{0.2}Ni_{0.2}Co_{0.2}Zn_{0.2}Cu_{0.2})O$

Jiejuan Yan[1,2,#,*], Lingkong Zhang[1,#], Junxiu Liu[1], Nana Li[1], Nobumichi, Tamura[3], Bin Chen[1], Yu Lin[4], Wendy L. Mao[2,4], Hengzhong Zhang[1]

[1]*Center for High Pressure Science and Technology Advanced Research, Shanghai 201203, P. R. China*

[2]*Department of Geological Sciences, Stanford University, Stanford, California 94305, United States*

[3]*Advanced Light Source, Lawrence Berkeley National Laboratory, Berkeley, California 94720, United States*

[4]*Stanford Institute for Materials and Energy Sciences, SLAC National Accelerator Laboratory, Menlo Park, California 94025, United States*

*To whom correspondence should be addressed. E-mail: jjyan2018@gmail.com

Abstract

Jahn-Teller distortion commonly exists in Cu-containing complex oxides and remarkably changes the electronic property. However, how it functions to pressure in high-entropy oxides (HEOs) remains unknown. Here we studied pressure engineering on quenching the Jahn-Teller distortion in the $(Mg_{0.2}Ni_{0.2}Co_{0.2}Zn_{0.2}Cu_{0.2})O$ HEO and its effect on the electronic structure. Synchrotron X-ray diffraction demonstrate that the local structural distortion of the CuO_6 octahedral sublattice in the rocksalt-type $(Mg_{0.2}Ni_{0.2}Co_{0.2}Zn_{0.2}Cu_{0.2})O$ HEO is progressively reduced and the distorted structure evolves into a nearly ideal form with increasing pressure up to 40 GPa. Alternating current impedance and ultraviolet-visible absorption reveal a dramatic resistance drop by more than 3 orders of magnitude and an obvious bandgap decrease of ~0.1 eV, accompanied by the pressure-induced quenching of the Jahn-Teller distortion in the $(Mg_{0.2}Ni_{0.2}Co_{0.2}Zn_{0.2}Cu_{0.2})O$ HEO. Our study presents a high-pressure route for tuning the local structural distortion and electronic structure of Cu-containing HEOs for optimizing the materials functionality.

HEOs is one type of recently discovered materials made up of five or more different oxides with roughly equal atomic ratio in compositions in a single solid solution phase, inspired by the synthesis concept of high-entropy alloys[1-5]. Several types of HEOs have been synthesized, including rocksalt type[5], CaF_2 type[6], spinel type[7], perovskite type[8] and even amorphous type[9]. Considerable experimental and theoretical efforts have been devoted to studying their structural stability and rich variety of physical properties that are promising for novel applications in a broad range of fields. Colossal dielectric constant has been observed in HEOs at a wide frequency regime, which is desired for large-k dielectric material[10]. Superionic lithium and sodium conductivity have also been observed in lithium or sodium doped HEOs[11,12], making them competitive candidates as electrolyte materials in lithium and sodium batteries.

Rocksalt-type HEOs is the first synthesized type of HEOs and have attracted extensive scientific interest. At ambient conditions, they crystallize into a *Fm*-3*m* structure with metal cations randomly distributed on the 4a position and oxygen anions occupied the 4b position of the face-centered cubic lattice[5]. Each metal cation is six-coordinated by oxygen anions to form a metal-O_6 octahedra, which further connects through edge-sharing and extends into a three-dimensional structure. In some Cu-containing rocksalt-type HEOs, such as $Mg_{0.2}Ni_{0.2}Co_{0.2}Zn_{0.2}Cu_{0.2}O$, the CuO_6 octahedra is usually distorted due to the Jahn-Teller effect[6,13-16]. Such structural distortion is highly sensitive to the synthesis and quenching conditions[16]. While the local structural distortion does not change the lattice symmetry, the relative intensities

of diffraction peaks are obviously changed. For instance, for rocksalt-type $(Mg_{0.2}Ni_{0.2}Co_{0.2}Zn_{0.2}Cu_{0.2})O$ HEO without distortion, (200) diffraction peak is the strongest and the intensity ratio of (111) and (200) peaks (I_{111}/I_{200}) is about 0.67 [16]. Jahn-Teller distortion of the CuO_6 octahedra will cause the (111) diffraction peak to be the strongest ($I_{111}/I_{200} > 1$)[16]. The full widths at half maximum (FWHM) of (111) and (200) peaks are also found to be different. Furthermore, the local structural distortion also dramatically changes the mechanical and physical properties of HEOs[10,13].

Pressure has been proven to be an effective approach to tune atomic distances, providing an alternative degree of freedom to optimize/design desired phases in HEOs. Recently, pressure-driven lattice distortion have been reported in the ideal rocksalt-type $(Mg_{0.2}Ni_{0.2}Co_{0.2}Zn_{0.2}Cu_{0.2})O$ and $(Ce_{0.2}La_{0.2}Pr_{0.2}Sm_{0.2}Y_{0.2})O^{2-\delta}$ HEOs without distortion[17,18]. While a few high-pressure studies focused on the structural stability and compressibility of HEOs in an ideal rocksalt-type structure[17-19], how compression tunes the local structural distortion caused by the Jahn-Teller effect in Cu-containing HEOs is less studied. Moreover, Jahn-Teller distortion can significantly change the electronic structure of CuO_6 sublattice[20-23]. Normally, the d^9 electronic configuration of Cu gives three electrons in the two degenerate e_g orbitals and causes a doubly degenerated ground state[23]. Jahn-Teller effect will break these orbital degeneracies and localize the e_g electrons. How will the electronic structure be tuned when the Jahn-Teller distortion in Cu-containing HEOs is quenched? Hence, pressure engineering of the Jahn-Teller distortion and its

relation to the electronic structure of Cu-containing HEOs represent an unexplored project.

In this work, we studied how compression tunes the Jahn-Teller distortion and the electronic structure of $Mg_{0.2}Ni_{0.2}Co_{0.2}Zn_{0.2}$ $Cu_{0.2}O$ HEO using synchrotron X-ray diffraction (XRD), alternating current (AC) impedance and ultraviolet-visible (UV-Vis) absorption measurements. With application of pressure up to 40 GPa, the Jahn-Teller distortion of CuO_6 octahedral sublattice in the rocksalt-type $(Mg_{0.2}Ni_{0.2}Co_{0.2}Zn_{0.2}Cu_{0.2})O$ HEO is progressively reduced and the distorted structure evolves into a nearly ideal form, accompanied by pronounced electrical resistance and optical bandgap decreases.

$(Mg_{0.2}Ni_{0.2}Co_{0.2}Zn_{0.2}Cu_{0.2})O$ HEO was synthesized using the previously reported solid-state reaction method[5,19]. Element mapping results obtained from the scanning electron microscopy (Figure 1(a)) show that all the elements are uniformly distributed. We studied the structural evolution of $(Mg_{0.2}Ni_{0.2}Co_{0.2}Zn_{0.2}Cu_{0.2})O$ HEO as a function of pressure up to 39.8 GPa at room temperature in a symmetric diamond anvil cell with Boehler-type diamonds (Figure 1(b)). At 2.9 GPa, the diffraction pattern can be well indexed into a rocksalt-type structure (*Fm*-3*m* symmetry) with lattice parameter $a = 4.223 \pm 0.004$ Å, comparable with previous result[24]. With applying the pressure up to 39.8 GPa, all the diffraction peaks shift to higher diffraction angles, and no new peak appears in the entire compression process, indicating that $(Mg_{0.2}Ni_{0.2}Co_{0.2}Zn_{0.2}Cu_{0.2})O$ HEO is stable at high pressure. The unit cell volume decreases smoothly with pressure without any collapse up to 39.8 GPa. By fitting the

pressure-volume curve with a third-order Birch-Murnaghan equation of state, a bulk modulus of 166.8 GPa with the pressure derivative of 4.2 is obtained, comparable with previous study on ideal rocksalt-type $(Mg_{0.2}Ni_{0.2}Co_{0.2}Zn_{0.2}Cu_{0.2})O$ HEO[17].

An interesting observation is that while the $(Mg_{0.2}Ni_{0.2}Co_{0.2}Zn_{0.2}Cu_{0.2})O$ HEO remains in the rocksalt-type *Fm*-3*m* structure, the relative peak intensities vary dramatically with pressure. At 2.9 GPa, the relative intensities of the diffraction peaks obviously deviate from the simulated pattern of an ideal rocksalt-type structure with a random distribution of the metal cations on the 4a position of face-centered cubic lattice (blue line in the bottom of Figure 1), and the previously reported XRD of an ideal rocksalt-type $(Mg_{0.2}Ni_{0.2}Co_{0.2}Zn_{0.2}Cu_{0.2})O$ HEO[17]. Instead of the (200) diffraction peak in the simulated pattern, the (111) peak is the strongest in our experimental results. With further compression up to above 21.9 GPa, the (200) peak becomes the strongest and the diffraction patterns are consistent with the simulated pattern of an ideal rocksalt-type structure. The intensity deviation at 2.9 GPa is anomalous. All the elements are uniformly distributed in the studied samples (Figure 1(a)), thus ruling out inhomogeneous distribution of the metal cations as being the cause. Furthermore, the relative intensities evolves significantly with pressure, indicating that it is an intrinsic behavior of $(Mg_{0.2}Ni_{0.2}Co_{0.2}Zn_{0.2}Cu_{0.2})O$ HEO, rather than a result of possible unequal atomic ratio in compositions because which keeps invariant with pressure. The observed difference in the relative peak intensities is consistent with previous studies on $(Mg_{0.2}Ni_{0.2}Co_{0.2}Zn_{0.2}Cu_{0.2})O$ HEO[16], in which the Jahn-Teller distortion was found to play a key role in the intensity deviation, indicating that the Jahn-Teller distortion is

the case for our study.

We performed quantitative analysis of the peak intensity and FWHM ratios to study the evolution of the Jahn-Teller distortion in the distorted rocksalt-type $(Mg_{0.2}Ni_{0.2}Co_{0.2}Zn_{0.2}Cu_{0.2})O$ as function of pressure. The intensity and FWHM ratios of the (111) and (200) peaks, I_{111}/I_{200} and $FWHM_{111}/FWHM_{200}$, are shown in Figure 2. At 2.9 GPa, I_{111}/I_{200} is about 1.6, much higher than ~0.67, the value for an ideal rocksalt-type $(Mg_{0.2}Ni_{0.2}Co_{0.2}Zn_{0.2}Cu_{0.2})O$ HEO with the metal cations randomly distributed on the 4a position of face-centered cubic lattice. With continuous compression, I_{111}/I_{200} drops obviously and eventually approaches to 0.67 at ~39.8 GPa. This indicates that pressure drives the Jahn-Teller distortion in the $(Mg_{0.2}Ni_{0.2}Co_{0.2}Zn_{0.2}Cu_{0.2})O$ HEO to be quenched and the distorted structure evolves into a nearly ideal form. The $FWHM_{111}/FWHM_{200}$ also support the evolution of local structure. At 2.9 GPa, $FWHM_{111}/FWHM_{200}$ is about 0.44, that is, the width of the (111) diffraction peak is much smaller than that of the (200) peak, similar to previous results on a distorted $(Mg_{0.2}Ni_{0.2}Co_{0.2}Zn_{0.2}Cu_{0.2})O$ HEO[16]. With further compression, $FWHM_{111}/FWHM_{200}$ increases, and eventually approaches to 1, the value for an ideal rocksalt-type structure.

AC impedance spectra measurements were carried out to study the evolution of electronic structure in the distorted rocksalt-type $(Mg_{0.2}Ni_{0.2}Co_{0.2}Zn_{0.2}Cu_{0.2})O$ HEO during the process of pressure-induced quenching of the Jahn-Teller distortion. Figure 3(a) and (b) present the Z'' vs. Z' impedance results of $(Mg_{0.2}Ni_{0.2}Co_{0.2}Zn_{0.2}Cu_{0.2})O$ HEO as a function of pressure up to 42.7 GPa. Only one

arc that relates to the grain relaxation process is observed in the entire compression process, which collapses dramatically with increasing pressure. To quantitatively track the change of electrical transport properties in the distorted rocksalt-type $(Mg_{0.2}Ni_{0.2}Co_{0.2}Zn_{0.2}Cu_{0.2})O$ HEO, a commonly used equivalent circuit shown in the inset of Figure 3(c) was used to simulate the grain relaxation process and extract the grain resistances. An obvious break in the trend is observed before and after the critical pressure of ~21.2 GPa, where the intensity ratio I_{111}/I_{200} is approaching to 1.0. Below ~21.2 GPa ($I_{111}/I_{200} > 1$, i.e., the (111) diffraction peak is the strongest), the resistance of $(Mg_{0.2}Ni_{0.2}Co_{0.2}Zn_{0.2}Cu_{0.2})O$ HEO varies smoothly with pressure. Above ~21.2 GPa ($I_{111}/I_{200} < 1$, i.e., the (200) diffraction peak is the strongest), the resistance drops sharply by more than three orders of magnitude up to 42.7 GPa, indicating a pressure-induced bandgap decrease.

UV-Vis absorption confirm the bandgap decrease in the distorted rocaksalt-type $(Mg_{0.2}Ni_{0.2}Co_{0.2}Zn_{0.2}Cu_{0.2})O$ HEO under compression. With application of pressure, the absorbance spectrum remains nearly invariant up to 19.3 GPa, followed by an obvious decrease at high energy regime (2.4 – 3.0 eV) with further compression. An obvious absorption edge can be observed at 1.8 – 2.2 eV in all the absorbance spectra (Figure 4), indicating that $(Mg_{0.2}Ni_{0.2}Co_{0.2}Zn_{0.2}Cu_{0.2})O$ HEO has a direct bandgap. The value of the direct bandgap can be estimated from the Tauc plot[25]:

$$(A \cdot E)^2 \sim E\text{-}E_g$$

where A and E are the absorbance of sample and incident energy, respectively. By fitting the linear regime of the $(A \cdot E)^2$ vs E curve and extrapolating the line to $(A \cdot E)^2 =$

0, the E_g value of $(Mg_{0.2}Ni_{0.2}Co_{0.2}Zn_{0.2}Cu_{0.2})O$ HEO can be determined (upper inset of Figure 4). At 1.7 GPa, $(Mg_{0.2}Ni_{0.2}Co_{0.2}Zn_{0.2}Cu_{0.2})O$ HEO has a direct bandgap of 1.91 eV. The bandgap is pressure-independent up to 19.3 GPa, beyond which a pronounced drop is observed with further compression up to 42.3 GPa. The variation trend of bandgap is consistent with that of the resistance of the $(Mg_{0.2}Ni_{0.2}Co_{0.2}Zn_{0.2}Cu_{0.2})O$ HEO. Typically, bandgap decrease makes it easier for charge carrier transition from valence band maximum to conduction band minimum, and consequently decreases the resistance.

Both the grain resistances and optical bandgaps of the distorted rocksalt-type $(Mg_{0.2}Ni_{0.2}Co_{0.2}Zn_{0.2}Cu_{0.2})O$ HEO show an obvious transition at ~20 GPa, where the intensity ratio of the (111) and (200) peaks changes from $I_{111}/I_{200} > 1$ to $I_{111}/I_{200} < 1$, suggesting that they are closely related. As discussed in previous studies[16,21], Jahn-Teller distortion breaks the orbital degeneracies and localizes the e_g electrons of Cu. Under compression, the distorted CuO_6 octahedra in the rocksalt-type $(Mg_{0.2}Ni_{0.2}Co_{0.2}Zn_{0.2}Cu_{0.2})O$ HEO evolves into a less distorted state and drives the delocalization of e_g electrons. Below the critical pressure, such as ~20 GPa in distorted rocksalt-type $(Mg_{0.2}Ni_{0.2}Co_{0.2}Zn_{0.2}Cu_{0.2})O$ HEO, the pressure-induced quenching of the Jahn-Teller distortion is not enough and the e_g electrons is not sufficiently delocalized, hence, the grain resistances and optical bandgaps are pressure-independent. With continuous compression to above ~20 GPa, the Jahn-Teller distortion is further suppressed, and the distorted structure progressively evolves into a nearly ideal cubic form, driving the e_g electrons become more delocalized. Consequently, the grain

resistances and optical bandgaps show a pronounced drop. Similar transition has also been observed in transition-metal oxide perovskites[21,26-28], although whether the Jahn-Teller distortion is fully suppressed at high pressure is still under debate.

In summary, by combing the XRD, AC impedance and UV-Vis absorption measurements, we studied the pressure engineering of quenching the Jahn-Teller distortion in the rocksalt-type $(Mg_{0.2}Ni_{0.2}Co_{0.2}Zn_{0.2}Cu_{0.2})O$ HEO, and its relation to the electronic structure. With application of pressure up to 40 GPa, the Jahn-Teller distortion in the rocksalt-type $(Mg_{0.2}Ni_{0.2}Co_{0.2}Zn_{0.2}Cu_{0.2})O$ HEO is progressively reduced and the distorted structure evolves into a nearly ideal form. The quenching of local structural distortion gives rise to a pronounced resistance drop by more than 3 orders of magnitude. Distorted rocksalt-type $(Mg_{0.2}Ni_{0.2}Co_{0.2}Zn_{0.2}Cu_{0.2})O$ HEO is a semiconductor with direct bandgap of ~1.91 eV, and the bandgap decreases to ~1.8 eV at 42.3 GPa following effective quenching of the local structural distortion. Our study presents a high-pressure route for tuning the Jahn-Teller distortion and electronic structure of Cu-containing HEOs for designing desired phases with improved materials functionality.

Experimental Section

Sample synthesis. $(Mg_{0.2}Ni_{0.2}Co_{0.2}Zn_{0.2}Cu_{0.2})O$ HEO was synthesized using the previously reported solid-state reaction method[5,19]. Solid MgO, CoO, NiO, CuO, and ZnO powders were mixed with an equal atomic ratio in compositions in an agate mortar and then ground for 6 h to make the oxides mixed uniformly and randomly.

The well-mixed powders were then compressed into a sheet with diameter of ~10 mm and thickness of ~1 mm using a hydraulic pressor to 300 MPa. The sheet was then heated up to 1100 °C in air for 3 h using a tube furnace, followed by quenching to room temperature in air by tuning off the tube furnace. Black $(Mg_{0.2}Ni_{0.2}Co_{0.2}Zn_{0.2}Cu_{0.2})O$ HEO powders were then obtained.

XRD measurements. High-pressure XRD measurements were conducted at the beamline 12.2.2 of Advanced Light Source (ALS), Lawrence Berkeley National Laboratory (LBNL) and Cornell High Energy Synchrotron Source (CHESS) with the X-ray wavelengths of 0.4959 Å and 0.4859 Å, respectively. MAR345 image plate was used to collect the diffraction patterns. The obtained two-dimensional (2D) images were then integrated to intensity vs diffraction angle (2θ) data using the Dioptas software[29]. Powdered $(Mg_{0.2}Ni_{0.2}Co_{0.2}Zn_{0.2}Cu_{0.2})O$ HEO samples, along with a small ruby ball (~5 μm in diameter) as pressure calibrant were loaded into a 150-μm-diameter sample chamber and compressed using a 300-μm culet (Boehler-type diamond) symmetric diamond anvil cell. Methanol-ethanol (4:1) was loaded as the pressure-transmitting medium. The peak intensities and FWHM were analyzed using the Lorenz function in the Origin software.

AC impedance measurements. High-pressure AC impedance measurements were performed by applying an AC voltage signal, $U(\omega,t)=U_0\cos(\omega,t)$, to the samples, and then detecting the response current signal on the samples, $I(\omega,t)=I_0\cos(\omega,t-\gamma)$[30]. The

impedance was then calculated by $Z^* = U/I = Z' + iZ''$. A two-electrodes configuration was used in our experiments. To insulate the metal gasket with the probing electrodes, an insulating cubic born nitride (c-BN) layers was prepared on the gasket by[31]: pre-indenting an T301 steel gasket to 40 um in thickness; drilling a 200-um hole in the center of the pre-indented area; pressing pre-mixed c-BN and epoxy powders (10:1 in weight) into the pre-indented area; and drilling a new 100-um hole in the center as sample chamber. No pressure-transmitting medium was loaded to make good contacts with the samples. A frequency range from 0.01 Hz to 10 MHz was set using a computer-controlled impedance analyzer (Solartron 1260) and a dielectric interface (Solartron 1296). A voltage signal with amplitude of 0.2 V was applied to the samples.

UV-Vis absorption measurements. High-pressure UV-Vis absorption measurements were conducted on a customized UV-Vis microscope system with a photon energy of 1.4 - 4.9 eV[32]. IIa-type diamond anvils were used in our absorption measurements. KBr was used as the pressure-transmitting medium. To subtract the background from diamond and pressure-transmitting medium, the transmittance of sample was obtained by two measurements, one being through the sample and the other through the pressure-transmitting medium beside the sample.

Acknowledgements

The research was supported by the National Natural Science Foundation of China (Grant 21875005). Contribution by Y.L. and W.L.M to the experiments, data analysis, and manuscript revising were supported by the U.S. Department of Energy, Office of Science, Basic Energy Sciences, Materials Sciences and Engineering Division (DE-AC02-76SF00515). We thank Martin Kunz and Jinyuan Yan of Beamline 12.2.2 at the Advanced Light Course (ALS) for experimental assistance. Beamline 12.2.2 at the ALS is a DOE Office of Science User Facility under contract No. DE-AC02-05CH11231.

References

(1) Yeh, J. W.; Chen, S. K.; Lin, S. J.; Gan, J. Y.; Chin, T. S.; Shun, T. T.; Tsau, C. H.; Chang, S. Y. Nanostructured high-entropy alloys with multiple principal elements: novel alloy design concepts and outcomes. *Adv. Eng. Mater.* **2004,** *6*, 299–303.

(2) Cantor, B.; Chang, I.; Knight, P.; Vincent, A. Microstructural development in equiatomic multicomponent alloys. *Mater. Sci. Eng. A* **2004,** *375*, 213–218.

(3) Zhang, Y.; Zuo, T. T.; Tang, Z.; Gao, M. C.; Dahmen, K. A.; Liaw, P. K.; Lu, Z. P. Microstructures and properties of high-entropy alloys. *Prog. Mater. Sci.* **2014,** *61*, 1–93.

(4) Ye, Y.; Wang, Q.; Lu, J.; Liu, C.; Yang, Y. High-entropy alloy: challenges and prospects. *Mater. Today* **2016,** *19*, 349–362.

(5) Rost, C. M.; Sachet, E.; Borman, T.; Moballegh, A.; Dickey, E. C.; Hou, D.; Jones, J. L.; Curtarolo, S.; Maria, J.-P. Entropy-stabilized oxides. *Nat. Commun.* **2015,** *6*, 8485-1–8485-8.

(6) Djenadic, R.; Sarkar, A.; Clemens, O.; Loho, C.; Botros, M.; Chakravadhanula, V. S.; Kübel, C.; Bhattacharya, S. S.; Gandhi, A. S.; Hahn, H. Multicomponent equiatomic rare earth oxides. *Mater. Res. Lett.* **2017,** *5*, 102–109.

(7) Dąbrowa, J.; Stygar, M.; Mikuła, A.; Knapik, A.; Mroczka, K.; Tejchman, W.; Danielewski, M.; Martin, M. Synthesis and microstructure of the (Co, Cr, Fe, Mn, Ni)$_3$O$_4$ high entropy oxide characterized by spinel structure. *Mater. Lett.* **2018,** *216*, 32–36.

(8) Sarkar, A.; Djenadic, R.; Wang, D.; Hein, C.; Kautenburger, R.; Clemens, O.; Hahn, H. Rare earth and transition metal based entropy stabilised perovskite type oxides. *J. Eur. Ceram. Soc.* **2018,** *38*, 2318–2327.

(9) Zhang, J.; Zhang, X.; Li, Y.; Du, Q.; Liu, X.; Qi, X. High-entropy oxides 10La$_2$O$_3$-20TiO$_2$-10Nb$_2$O$_5$-20WO$_3$-20ZrO$_2$ amorphous spheres prepared by containerless solidification. *Mater. Lett.* **2019,** *244*, 167–170.

(10) Bérardan, D.; Franger, S.; Dragoe, D.; Meena, A. K.; Dragoe, N. Colossal dielectric constant in high entropy oxides. *Phys. Status Solidi RRL* **2016,** *10*, 328–333.

(11) Sarkar, A.; Velasco, L.; Wang, D.; Wang, Q.; Talasila, G.; de Biasi, L.; Kübel, C.; Brezesinski, T.; Bhattacharya, S. S.; Hahn, H.; et al. High entropy oxides for reversible energy storage. *Nat. Commun.* **2018,** *9*, 3400-1–3400-9.

(12) Bérardan, D.; Franger, S.; Meena, A.; Dragoe, N. Room temperature lithium superionic conductivity in high entropy oxides. *J. Mater. Chem. A* **2016,** *4*, 9536–9541.

(13) Anand, G.; Wynn, A. P.; Handley, C. M.; Freeman, C. L. Phase stability and distortion in high-entropy oxides. *Acta Mater.* **2018,** *146*, 119–125.

(14) Rost, C. M.; Rak, Z.; Brenner, D. W.; Maria, J. P. Local structure of the Mg$_x$Ni$_x$Co$_x$Cu$_x$Zn$_x$O (x=0.2) entropy-stabilized oxide: an EXAFS study. *J. Am. Ceram. Soc.* **2017,** *100*, 2732–2738.

(15) Rak, Z.; Rost, C.; Lim, M.; Sarker, P.; Toher, C.; Curtarolo, S.; Maria, J.-P.;

Brenner, D. Charge compensation and electrostatic transferability in three entropy-stabilized oxides: Results from density functional theory calculations. *J. Appl. Phys.* **2016,** *120*, 095105-1–095105-11.
(16) Berardan, D.; Meena, A.; Franger, S.; Herrero, C.; Dragoe, N. Controlled Jahn-Teller distortion in (MgCoNiCuZn)O-based high entropy oxides. *J. Alloys Compd.* **2017,** *704*, 693–700.
(17) Cheng, B.; Lou, H.; Sarkar, A.; Zeng, Z.; Zhang, F.; Chen, X.; Tan, L.; Glazyrin, K.; Yan, J.; Wang, L.; et al. Lattice distortion and stability of ($Co_{0.2}Cu_{0.2}Mg_{0.2}Ni_{0.2}Zn_{0.2}$)O high-entropy oxide under high pressure. *Mater. Today* **2020,** *8*, 100102-1–100102-10.
(18) Cheng, B.; Lou, H.; Sarkar, A.; Zeng, Z.; Zhang, F.; Chen, X.; Tan, L.; Prakapenka, V.; Greenberg, E.; Wen, J.; et al. Pressure-induced tuning of lattice distortion in a high-entropy oxide. *Commun. Chem.* **2019,** *2*, 114-1–114-9.
(19) Chen, J.; Liu, W.; Liu, J.; Zhang, X.; Yuan, M.; Zhao, Y.; Yan, J.; Hou, M.; Yan, J.; Kunz, M.; et al. Stability and compressibility of cation-doped high-entropy oxide $MgCoNiCuZnO_5$. *J. Phys. Chem. C* **2019,** *123*, 17735–17744.
(20) Kyono, A.; Gramsch, S. A.; Nakamoto, Y.; Sakata, M.; Kato, M.; Tamura, T.; Yamanaka, T. High-pressure behavior of cuprospinel $CuFe_2O_4$: Influence of the Jahn-Teller effect on the spinel structure. *Am. Mineral.* **2015,** *100*, 1752–1761.
(21) Loa, I.; Adler, P.; Grzechnik, A.; Syassen, K.; Schwarz, U.; Hanfland, M.; Rozenberg, G. K.; Gorodetsky, P.; Pasternak, M. P. Pressure-Induced Quenching of the Jahn-Teller Distortion and Insulator-to-Metal Transition in $LaMnO_3$. *Phys. Rev. Lett.* **2001,** *87*, 125501-1–125501-4.
(22) Sturge, M. The Jahn-Teller effect in solids. In *Solid State Physics*, Elsevier: 1968; Vol. 20, pp 91–211.
(23) Rák, Z.; Maria, J.-P.; Brenner, D. Evidence for Jahn-Teller compression in the (Mg, Co, Ni, Cu, Zn)O entropy-stabilized oxide: A DFT study. *Mater. Lett.* **2018,** *217*, 300–303.
(24) Sarkar, A.; Djenadic, R.; Usharani, N. J.; Sanghvi, K. P.; Chakravadhanula, V. S.; Gandhi, A. S.; Hahn, H.; Bhattacharya, S. S. Nanocrystalline multicomponent entropy stabilised transition metal oxides. *J. Eur. Ceram. Soc.* **2017,** *37*, 747–754.
(25) Tauc, J. Optical properties and electronic structure of amorphous Ge and Si. *Mater. Res. Bull.* **1968,** *3*, 37–46.
(26) Baldini, M.; Struzhkin, V. V.; Goncharov, A. F.; Postorino, P.; Mao, W. L. Persistence of Jahn-Teller Distortion up to the Insulator to Metal Transition in $LaMnO_3$. *Phys. Rev. Lett.* **2011,** *106*, 066402-1–066402-4.
(27) Ruiz-Fuertes, J.; Segura, A.; Rodríguez, F.; Errandonea, D.; Sanz-Ortiz, M. N. Anomalous High-Pressure Jahn-Teller Behavior in $CuWO_4$. *Phys. Rev. Lett.* **2012,** *108*, 166402-1–166402-4.
(28) Aguado, F.; Rodriguez, F.; Núñez, P. Pressure-induced Jahn-Teller suppression and simultaneous high-spin to low-spin transition in the layered perovskite $CsMnF_4$. *Phys. Rev. B* **2007,** *76*, 094417-1–094417-6.
(29) Prescher, C.; Prakapenka, V. B. DIOPTAS: a program for reduction of two-dimensional X-ray diffraction data and data exploration. *High Press. Res.* **2015,** *35*,

223–230.
(30) Schmidt, R.; Wu, J.; Leighton, C.; Terry, I. Dielectric response to the low-temperature magnetic defect structure and spin state transition in polycrystalline $LaCoO_3$. *Phys. Rev. B* **2009,** *79*, 125105-1–125105-8.
(31) Ke, F.; Dong, H.; Chen, Y.; Zhang, J.; Liu, C.; Zhang, J.; Gan, Y.; Han, Y.; Chen, Z.; Gao, C.; et al. Decompression-Driven Superconductivity Enhancement in In_2Se_3. *Adv. Mater.* **2017,** *29*, 1701983-1–1701983-5.
(32) Ke, F.; Zhang, L.; Chen, Y.; Yin, K.; Wang, C.; Tzeng, Y.-K.; Lin, Y.; Dong, H.; Liu, Z.; Tse, J. S.; et al. Synthesis of atomically thin hexagonal diamond with compression. *Nano Lett.* **2020,** *20*, 5916–5921.

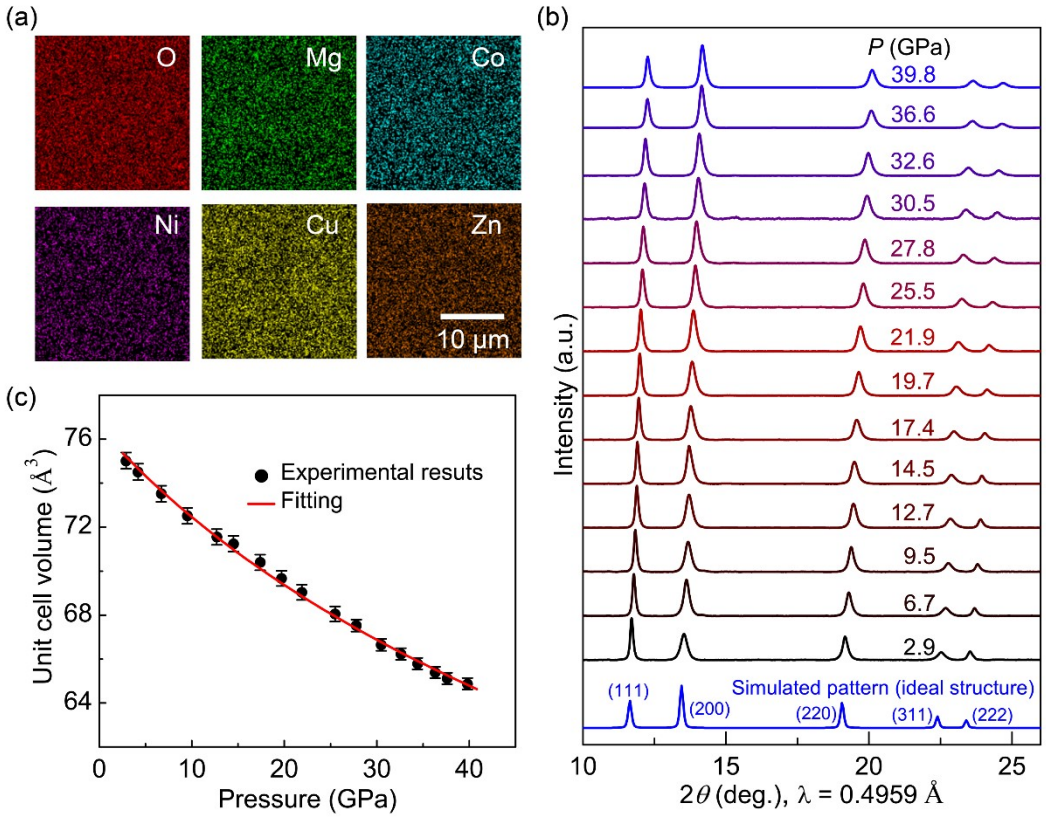

Figure 1. (a) Element mapping of distorted rocksalt-type $(Mg_{0.2}Ni_{0.2}Co_{0.2}Zn_{0.2}Cu_{0.2})O$ HEO obtained from the scanning electron microscope. (b) XRD patterns of distorted rocksalt-type $(Mg_{0.2}Ni_{0.2}Co_{0.2}Zn_{0.2}Cu_{0.2})O$ HEO at representative pressures showing the structural stability. (c) pressure dependence of unit cell volume of $(Mg_{0.2}Ni_{0.2}Co_{0.2}Zn_{0.2}Cu_{0.2})O$ HEO. The black solid cycles and red line are the experimental data and fitted curve based on the third-order Birch–Murnaghan equation of state, respectively.

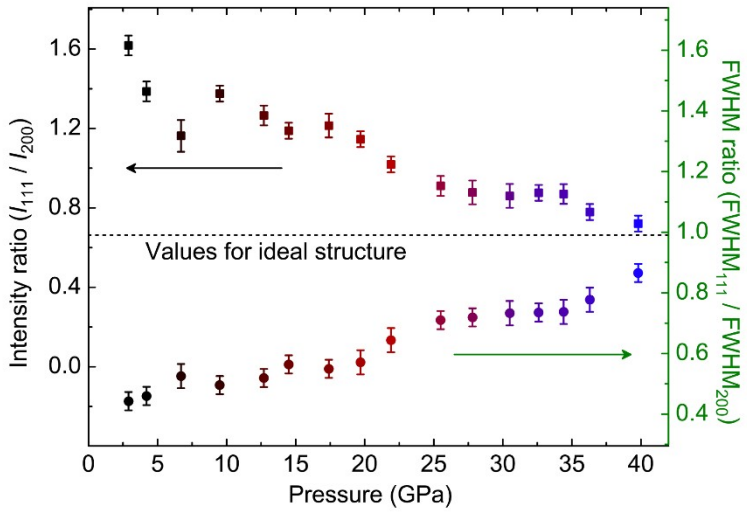

Figure 2. Intensity and FWHM ratios of the (111) and (200) diffraction peaks of distorted rocksalt-type $(Mg_{0.2}Ni_{0.2}Co_{0.2}Zn_{0.2}Cu_{0.2})O$ HEO, I_{111}/I_{200} and $FWHM_{111}/FWHM_{200}$, as a function of pressure. The dashed line are the values for an ideal rocksalt-type $(Mg_{0.2}Ni_{0.2}Co_{0.2}Zn_{0.2}Cu_{0.2})O$ HEO with a random distribution of the cations on the 4a position of face-centered cubic lattice. The error bars are from the fitting uncertainty of peak intensities and FWHM.

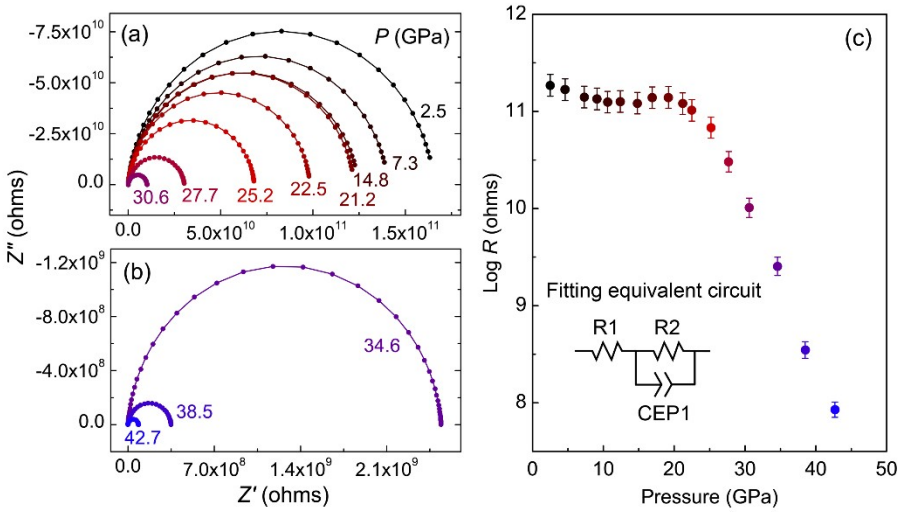

Figure 3. (a)-(b) Impedance spectra of distorted rocksalt-type $(Mg_{0.2}Ni_{0.2}Co_{0.2}Zn_{0.2}Cu_{0.2})O$ HEO under compression. (c) The grain resistance as a function of pressure obtained by fitting the $Z' - Z''$ plots using the equivalent circuit in the inset.

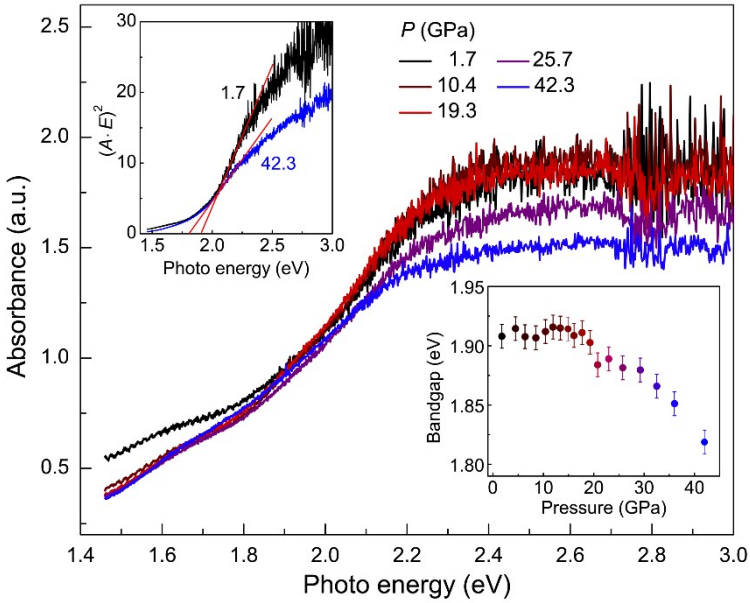

Figure 4. Absorbance of distorted rocksalt-type $(Mg_{0.2}Ni_{0.2}Co_{0.2}Zn_{0.2}Cu_{0.2})O$ HEO under compression. The upper inset presents the $(A{\cdot}E)^2$ vs E curves at 1.7 and 42.3 GPa for bandgap fitting. The bottom inset shows the evolution of direct bandgap as a function of pressure.